Article

Effects of tropospheric emissions on global tropospheric ozone distribution: A CTM simulation study

Kuo-Ying Wang

Department of Atmospheric Sciences, National Central University, Chung-Li, Taiwan

* Author to whom correspondence should be addressed; kuoying@mail.atm.ncu.edu.tw,
+886-3-280-4420.

Abstract: In this work, we examined the effect of tropospheric emissions on tropospheric ozone (O_3) by conducting three-dimensional (3D) chemistry transport model (CTM) simulations. For the control run, the CTM model simulates tropospheric O_3 levels with a complete set of anthropogenic, biomass burning, and vegetation emissions [8]. For the no-emission simulation, all anthropogenic, biomass burning, and vegetation emissions were turned off. Comparisons of results from these two simulations exhibit the emission impacts on the tropospheric O_3. In the no-emission simulation, distinctive low surface O_3 with concentrations less than 5 ppbv prevail over the Amazon basin, tropical South America, tropical South Africa, Southeast Asia. Transport of air from these land areas downwind contributes to the low O_3 over the remote marine boundary layer. In contrast, elevated O_3 levels over the extra-tropical remote marine boundary layer are less supported by the anthropogenic and biomass burning emissions but more sustained by the downward transport of O_3 from the stratosphere. These results demonstrate that the northern hemisphere continental areas (north of $30°N$), polar regions, and tropical continental regions are more sensitive to the tropospheric emissions. The northern hemisphere winter is mostly dominated by the stratospheric processes, while the tropospheric emissions dominate over the southern hemisphere tropical continental areas from tropics to $30°S$ latitudinal bands. The northern hemisphere continental regions are increasingly dominated by tropospheric emissions from spring, to reach maxima in summer, and started to reduce in autumn months.

Keywords: tropospheric emissions; CTM; tropospheric ozone; industrial emissions; biomass buring; vegetation emissions; simulation

doi:10.20944/preprints201706.0091.v1

1. Introduction

Atmospheric O_3 exhibit a near order two of magnitude change from the upper troposphere to the lower stratosphere. The omnipresence of the steep vertical gradient in O_3 and active stratospheric-tropospheric exchange process affect O_3 in the troposphere on a seasonal and global scales [1].

On the other hand, tropospheric emissions exert a direct impact on the tropospheric O_3 concentrations. The emissions from man-made industrial sources such as nitrogen oxides (NOx), hydrocarbons, carbon monoxide (CO), biomass burning activities, and vegetation emissions [2;3;4;5;6;7;8] are the main sources of primary emissions for the photochemical productions of O_3 in the troposphere. These emissions are local in nature, mainly concentrated in the continental areas of both hemispheres.

How are these two effects, one from above the troposphere and the other one from below the troposphere, compete to dominate local tropospheric O_3 on a seasonal and global scale? [9;10].

There are two views regarding the source of the photochemical processes in the troposphere contributing to the tropospheric O_3 concentrations. First, wintertime accumulation of O_3 producing precursors over the continental industrial areas where anthropogenic emissions have a longer chemical lifetime than other seasons. Also, the major sinks for O_3, species such as hydrogen oxides (HOx) and water (H_2O), are low during the winter, hence more O_3 can accumulate in high latitudes than other seasons. The accumulation of O_3 precursors and O_3 from the stratosphere give rise to the northern hemisphere springtime O_3 maximum [11;12;7]. Also, long-range transport of continental pollutants provides another source of elevated O_3 and other pollution over the remote marine boundary layer [13;12;14].

Second, the timing of the spring O_3 maximum coincides with the period of the most active biomass burning in the tropical and subtropical regions. Biomass burning emissions emit O_3 producing precursors. Long-range transport and cloud convective transport processes transport these O_3 precursors to the remote atmosphere. These are the major driving force of the southern hemisphere spring O_3 maximum [15;16;17;18;7].

Two approaches are used to access the impact of the photochemical production of O_3 in the troposphere. First, the stratospheric tracer approach. By using a marked stratospheric O_3 tracer, the difference between the O_3 concentrations from full chemistry integrations and the O_3 from stratospheric tracer is calculated as the O_3 that originates from photochemistry in the troposphere [19;20;12;7;5]. *Roelofs et al.* [19] calculated that 30% of O_3 in the troposphere derived from anthropogenic emission of O_3 producing precursors and natural photochemical production, respectively, and the stratosphere contributed about 40% of O_3 in the troposphere.

Second, the emission approach. *Lelieveld and Dentener* [7] experimented various emission scenarios to access present day polluted O_3 levels to that of O_3 from a preindustrial period. *Lelieveld and Dentener* [7] estimated that industrial and fossil-fuel related emissions strongly affected tropospheric O_3 in the extra-tropical northern hemisphere, while natural emissions play a significant role in the tropics and southern hemisphere. They calculated that man-made biomass burning emissions contribute 10% to 15% to the tropospheric ozone column in the tropical latitudes.

In this work, we present a study on the impact of tropospheric O_3 from tropospheric emissions. We conducted and compare results from simulations based on various scenarios of tropospheric emissions and stratospheric influences against control run. These comparisons reveal the temporal and spatial distribution of tropospheric effects and stratospheric effect on tropospheric O_3 concentrations on a global scale.

2. Methods

2.1. The IMS CTM Model

The Integrated Modeling System (IMS) three-dimensional (3D) tropospheric chemistry transport model (CTM) is used in this work [8;21;22]. The model uses a general gas-phase reaction mechanism for NOx, methane, non-methane hydrocarbon (NMHC), biogenic volatile organic compounds (VOCs), and some sulfur and halogen reactions [22]. The IMS model used specified surface emissions for anthropogenic sources from Emission Database for Global Atmospheric Research (EDGAR) and Global Emission InitiAtive (GEIA) [22]. The model was driven by analyzed winds from European Centre for Medium-Range Weather Forecast (ECMWF), and it contains 19 vertical layers which extend from surface to about 10 hPa. The horizontal resolution for the model is 7.5 by 4.5-degree longitude-latitude. The concentrations of O_3, reactive nitrogen (NOy), and nitric acid (HNO_3) in the stratosphere are prescribed similarly to the method of *Berntsen and Isaksen* [23].

2.2. List of CTM Simulation Experiments

To study the effect of tropospheric emissions on the levels of O_3 in the troposphere, we conduct simulations with various emission scenarios as shown in Table 1.

The industrial emissions include emissions of CO, hydrocarbons, and NOx. We note that the NOx emissions include fossil fuel-related emissions, lightning, and soil process. Hence, there is no major O_3 photochemical sources (e.g., biomass burning, fossil fuel burning, lightning, soil process) included in the simulation.

Biogenic sources paly a vital role in affecting tropospheric O_3 via the emissions of biogenic hydrocarbons and NOx [25;18;22].

For comparison of the stratospheric effects, we performed simulations with different stratospheric fluxes on tropospheric O_3 concentrations. We test the stratospheric influxes of O_3 and NOy [26] on O_3 levels in the troposphere.

2.3. Simulation Setup and Platform

The IMS model run two years of simulations for each scenario shown in Table 1. The model used the 6-hourly meteorological analysis from the ECMWF analysis for the period 1991-1992, and output

Table 1. List of CTM Scenarios Simulated in This Work.

Scenario	Description
5	Control run
	Simulations of Downward influences
7	Long-lived O_3 tracer experiment: No stratospheric O_3 fluxes and tropospheric chemistry; O_3 in the tropopause regions and in the stratosphere were constantly set to 100 ppbv; O_3 concentrations in the troposphere were reset to initial conditions every hour
8	No stratospheric O_3
22	No stratospheric O_3 and NOy fluxes
24	No stratospheric O_3 fluxes
28	Short-lived O_3 tracer experiment: Similar to experiment 7; Lifetime for tropospheric O_3 were set to 168 hours
	Simulations of Upward influences
11	No industrial and biomass burning emissions, but with vegetation emissions
14	No industrial industrial, biomass burning, and vegetation emissions
18	No vegetation emissions, but with industrial and biomass burning emissions
26	No industrial and biomass burning burning emissions; no stratospheric NOy fluxes
30	Doubled industrial emissions from Asian regions

t

simulation results in every 6 hours. This work used results from the second year in the discussion shown below. The IMS model performed simulations on a Cray J90 supercomputer at National Taiwan University (NTU).

The Cray J90 is a shared memory supercomputer, which enables codes to run on an ensemble of central processing unit (CPU) simultaneously with greater efficiency than traditional single CPU simulation method [24]. We specifically designed the IMS codes to match and benefit from the unique hardware and software mechanisms provided by the Cray J90. As such, the model run parallelly on the Cray J90 since 1995.

2.4. Results Analysis

We use O_3 ratios to exam the effect of a scenario simulation. For example, we divided tropospheric O_3 from a particular situation to the tropospheric O_3 from control run (the full model simulation). Hence, the O_3 ratios measure the effects that particular scenario.

For the scenario without tropospheric emissions, the variations of the O_3 ratios indicate the effect of O_3 in the troposphere from primary photochemical sources within the troposphere. An O_3 ratio with unity indicates that tropospheric photochemical sources produce no impact at all on the levels of O_3 in the troposphere. The smaller the O_3 ratios, the bigger the impact derived from the emission sources in the troposphere.

The comparisons were made at the surface using a time-series plot, and above the surface using a series of the zonal mean cross-sections for different seasons. We also compare different model simulations with surface and ozonesonde measurements to highlight the spatial and temporal distribution of the impact of O_3 from combustion-derived photochemical sources in the troposphere.

3. Results and Discussion

3.1. Comparison of Model with Surface Measurements

Figure 1 compares time-series plots of modeled O_3 from simulations with and without combustion emissions included, respectively, with observed O_3 levels at four sites located in the remote marine boundary layer. The simulation without the combustion emissions can reproduce the observed spring O_3 maximum at the surface similar to that shown in the measurements.

There are agreements and discrepancies in the levels of O_3 simulated between these two simulations. Close agreement between the simulations indicates that anthropogenic and pyrogenic emissions are of less importance, while the disagreements between the two simulations provide a measure of the contribution from photochemical production on O_3 in the troposphere. For example, the no-emission simulation at Westman Island shows close agreement between the model and the daily minimum measurements (Figure 1a). This indicates that background O_3 concentrations from the stratosphere mostly controls the variation of the daily observed lowest O_3 levels at this location.

The disagreements between the two model simulations occur from mid-spring to late summer. The timing of the maximum discrepancies occur in summer is consistent with the period when photochemical production in the troposphere is active. These characteristics between the two model calculations, close agreement in winter and differences in spring to summer, also occur at other locations in Figure 1.

Notice that in the no-emission simulation the O_3 maximum peaks in spring, instead of winter [20]. Notice also that the timing of peak O_3 maximum in the simulations occurs during April to June, slightly lags the no-emission simulation at these two sites (Westman Island, Figure 1a; and Bermuda, Figure 1b). These delays in the timing of peak spring O_3 maximum, due to anthropogenic emissions in the northern hemisphere industrial latitudes, can be used as a measure for assessing the impact of future NOx emission scenarios [7].

At Mauna Loa (Figure 1c), the no-emission model follows closely but slightly lower than the O_3 concentrations simulated when emissions were included. The higher O_3 calculated from the no-emission model compared with the observed daily minimum values indicates that the model overestimates O_3 from the stratosphere to the troposphere at this location. At Samoa (Figure 1d), the model without combustion emissions included follows closely the observed daily maximum O_3 levels. Additional O_3 production from photochemical processes, e.g., due to pyrogenic emissions from tropical continents, further enhances O_3 levels in the model at this site.

Notice that the higher surface O_3 from the no-emission calculation in late August (late winter in the southern hemisphere) than the emission included simulation. This phenomenon is due to the lower net O_3 photochemical loss in the former (without emissions) than the later (with emissions) simulations during this short period at this site.

3.2. Effect of no Emissions on Tropospheric O_3 Distribution

3.2.1. At the Ground Level

Figure 2a shows surface O_3 distribution simulated without combustion emissions included in the troposphere during the southern hemisphere spring months. The high surface O_3 (highlighted by the O_3=35 ppbv contour) is well maintained but with less widespread coverage over the southern hemisphere oceans in the model without emissions compared with the model with emissions included (Figure 2b).

The no-emission simulation presents the inter-hemispheric asymmetry in O_3 over the marine boundary layer. This pattern indicates downward transport of O_3 from the stratosphere mostly maintained the inter-hemispheric asymmetric of O_3.

In the northern hemisphere emission areas such as eastern U.S., Europe, and East Asia the model without emissions included shows that O_3 over these regions has reduced. For the tropical and the southern hemisphere regions such as South America, Central Africa, and Southeast Asia, these areas exhibit low O_3 concentrations in the model without emissions included. For example, less than 5 ppbv of O_3 occur over the Amazon basin, tropical Africa, and Southeast Asia.

Figure 2c shows surface O_3 concentrations from the run without to the run with emissions included for the southern hemisphere spring. Without photochemical source emissions in the troposphere, surface O_3 levels in the tropical and the southern hemisphere continental regions (close to intense biomass burning activities) are dramatically reduced to as low as about 20% in South America and Africa, and about 30% in Southeast Asia.

More than 90% of O_3 concentrations over the extra-tropics to the poleward latitudes of the southern Atlantic, the Indian, and the western Pacific oceans are maintained, even without biomass burning and NOx emissions from continental regions. A narrow band of the low O_3 ratios of about 70% extends from eastern U.S., across the tropical Atlantic, and reaches tropical Africa. On the western side of the tropical Pacific, low O_3 ratios of about 60% to 70% extend from Southeast Asian continent to central equatorial Pacific. These patterns illustrate the downwind influence of low O_3 from continental regions to the remote tropical marine boundary layer.

The reductions in O_3 concentrations between the equator and $10°S$ are 10% greater than in the latitudes between $10°S$ and $20°S$ in the southern Atlantic. These patterns indicate that regions over the tropical Atlantic are more likely to be influenced by O_3 photochemically produced from the tropical areas. Pronounced biomass burning emissions are known to be a dominating factor over tropical areas [15;16;18;3;17;2].

Figure 3 shows mean O_3 at surface without (Figure 3a) and with (Figure 3b) emissions for the March-April period. Both model simulations produce the distinctive patterns of inter-hemispheric asymmetry in the surface O_3 over the marine boundary layer. Surface O_3 concentrations from the model without emissions included are about $80\% - 90\%$ to the O_3 levels from the model with combustion emissions added over the northern hemisphere marine boundary layer(Figure 3c).

Continental regions such as the Amazon basin and South America, equatorial Africa, and Southeast Asia exhibit low levels of the surface O_3 in the model without combustion emissions included. The no-emission simulation calculated less than 5 ppbv of O_3 concentrations in some of these areas.

In addition to the lack of O_3 producing precursors in the no-combustion emissions model, high density terrestrial vegetation, which emits a large amount of volatile biogenic organic compounds such as isoprene and monoterpenes, reacts with O_3 in these area and causing a sharp reduction in O_3 concentrations [8].

In addition to the tropical and southern hemisphere continental areas where low surface O_3 exist, low surface O_3 ($\leq$ 15-20 ppbv) prevails over the tropical South Atlantic, the Indian, and the Pacific. As shown from the no-combustion model simulation (Figure 3a), low surface O_3 extends from tropical and southern hemisphere continental areas to the remote tropical and extra-tropical marine boundary layer. The surface distribution of the O_3 ratios (Figure 3c) shows a long narrow band of low values ($\leq 60 - 70\%$) over the remote tropical marine boundary layer, extending from continental areas where as low as less than 20% of the O_3 ratios exist. These results exhibit the influence of tropical and southern hemisphere continental air on the remote tropical and extra-tropical marine boundary layer.

We find that surface O_3 with concentrations less than 5 ppbv prevail over the Amazon basin, tropical South America, equatorial and tropical Africa, and Southeast Asia in the model without emissions included. Low O_3 concentrations over the remote marine boundary layer are associated with air low in O_3 transported from the clean tropical continental regions. On the other hand, high O_3 concentrations can be maintained over the extra-tropical remote marine boundary layer due to the downward transport of O_3 from the stratosphere.

This stratospheric influence supported the inter-hemispheric asymmetry in O_3 even if there are no combustion emissions included in the model.

3.2.2. Meridional Cross-Section

Figure 4 compares the zonal mean cross-section of the O_3 ratios, simulated without to those with emissions, in four seasons. During the northern hemisphere summer (Figure 4b), zonal mean O_3 ratios less than $60\% - 65\%$ can be seen in the tropical lower troposphere and the northern hemisphere lower troposphere at latitudes north of $30°N$, respectively. While low O_3 ratios in tropical regions indicate the influence of O_3 production from biomass burning emissions, low O_3 ratios in the mid to high latitudes illustrates the importance of photochemical O_3 production derived from anthropogenic emissions. These summertime low O_3 ratios in the northern hemisphere lower troposphere gradually increase as the season moves through to autumn (Figure 4c) to reach their highest values ($\geq 85\% - 95\%$)in the northern hemisphere winter troposphere (Figure 4d). The O_3 ratios greater than 95% in the latitudes north of $30°N$ and throughout the troposphere indicate the dominant contribution of O_3 from the stratosphere to the troposphere during the northern hemisphere winter [19].

Similar seasonal movements occur for the O_3 ratios in the southern hemisphere through summer (Figure 4d) to winter (Figure 4b). The vertical extent of the stratospheric dominance in the austral winter hemisphere is about 95% at altitudes between the tropopause and the mid-troposphere (500 hPa), and about $85\% - 95\%$ below the mid troposphere. A smaller stratospheric dominance in the austral winter lower troposphere compared with the boreal winter lower troposphere is consistent with less great winter mass influx from the stratosphere to the troposphere in the southern hemisphere than in northern hemisphere [27;6].

Hence, the stratosphere dominated the tropospheric O_3 in the winter hemisphere, while a mixture of both photochemical O_3 production and O_3 from the stratosphere controlled O_3 in the summer hemisphere.

As the northern hemisphere enters its spring season, Figure 4a shows a symmetry of the O_3 ratios between northern hemisphere and southern hemisphere. In the lowest part of the troposphere and at latitudes between $30°N$ and $45°N$ where low O_3 ratio indicates the gradual development of photochemical O_3 production from the low troposphere as the sun gradually returns to the northern hemisphere. In the meantime, the full photochemical production in the southern hemisphere summer has slowly faded away as the southern hemisphere enters its autumn. Therefore a longer-lived O_3 accumulated in the previous winter plus the return of the photochemical processes produce a tropospheric O_3 maximum in spring [20].

For the southern hemisphere spring (Figure 4c), the seasonal pyrogenic emissions of O_3 precursors in the southern hemisphere tropical continents fueled photochemical production.

3.3. Comparison of Model Ozone Profiles

3.3.1. The Atlantic Basin

Figure 5 compares time-height cross sections of modeled and measured O_3 profiles at a northern (Bermuda; Figures 5a and b) and a southern (Irene; Figures 5d and e) Atlantic sites. For the simulations without combustion emissions, distinctive spring maximum occur in the upper to middle troposphere at Bermuda (Figure 5a). These characters are similar to the measurements (Figure 5b). Vertical distribution of the O_3 ratios at this site (Figure 5c) show that about $85\% - 95\%$ of the northern hemisphere spring O_3 maximum can be reproduced by the model without considering combustion emission of O_3 precursors from continental areas [28;31]. Photochemical O_3 production becomes important in the lower troposphere during late spring to late summer seasons.

At Irene, the no-emission model shows a distinctive O_3 maximum in the troposphere during the southern hemisphere winter to spring seasons (Figure 5d). These patterns are similar to that of the measurements (Figure 5e). About $85\% - 95\%$ of O_3 in the troposphere at this site during the southern hemisphere winter and early spring can be maintained by the downward transport of O_3 from the stratosphere (Figure 5f). Low O_3 ratios (less than 80%) occur at this site during the southern hemisphere spring to summer months, from October to December and from January to March (Figure 5f).

These low O_3 ratios indicate that pyrogenic emissions play a major role in the lower troposphere. These results are consistent with previous analyses. Transport of photochemically produced O_3, due to biomass burning emissions and/or O_3 producing precursors from continents, is the major factor for elevated O_3 observed at this region [2;3;18].

3.3.2. Pacific Basin

Figure 6a shows time-height cross sections of vertical ozone profiles simulated without combustion emissions in the model at Taiwan, which is located in the subtropical western North Pacific. The model shows downward intrusion of elevated O_3 from the stratosphere to upper and the middle troposphere from February to May. The vertical extent of the elevated O_3 in the troposphere at this site is not as extensive as O_3 shown from the measurements during the same period (Figure 6b). High O_3 ratios (greater than 85%) occur during winter (December, January, and February; Figure 6c), indicating that the no-emission model can produce O_3 in the troposphere comparable with the model with emissions included.

On the other hand, development of the low O_3 ratios from spring to late summer and early autumn, and extends from the lower troposphere in spring to the whole troposphere in September. These patterns indicate that tropospheric photochemical production of O_3 plays a significant role in contributing to the observed O_3 maximum in spring and summer at this location. These characteristics are consistent with previous studies [29;30].

The no-emission model at Tahiti (Figure 6d) shows downward transport of O_3 from the stratosphere during the southern hemisphere winter. These modeled results are comparable with the measurements (Figure 6e). Ratios of O_3 close to unity at this site indicate that photochemical production in the troposphere is not a significant contributor to O_3 at this site (Figure 6f).

3.3.3. Northern Hemisphere Higher Latitudes

For locations at higher latitudes, the non-emission model shows the distinctive northern hemisphere spring O_3 maximum in the troposphere at Trinidad Head (Figure 7a) and Boulder (Figure 7d). These model results are close to the measurements (Figures 7b and e). Occurrences of high O_3 ratios (about 0.85-0.95; Figure 7c and f) indicate the significant role played by O_3 transported from the stratosphere in this region during the northern hemisphere spring. As the season enters summer, the dramatic reduction in the values of the O_3 ratios in the lower troposphere illustrate the importance of the tropospheric photochemical processes (Figure 7c and d). For example, the model without considering combustion emissions of O_3 precursors in the lower troposphere produced less than 50% of the surface O_3 at Boulder.

3.3.4. Comaprisons of Scenarios and Seasonal Variations

Previous sections showed that downward transport of elevated ozone from the upper troposphere and lower stratosphere regions, and upward transport of primary emissions from the surface affect ozone concentrations in the troposphere. In this section, we further test these two main effects, and exam seasonal variations of these effects on tropospheric ozone concentrations.

Figure 8 shows test results of ground-level O_3 distribution when the tropospheric chemistry (including photochemical sources and sinks, and deposition removal of O_3) turn off (experiment 7). As no photochemical processes exit for O_3, this is a long-lived O_3 tracer test. The simulation results show that O_3 from the tropopause regions fill the entire troposphere.

However, there exist spatial and temporal variabilities in the amount and distribution of elevated ozone been transported downward from the tropopause regions.

For the northern hemisphere winter months (DJF), the maximum ground-level O_3 concentrations occur around $30°N$. In the southern hemisphere, the highest ground-level O_3 concentrations occur around $20°S - 30°S$.

The western North America, western North Africa, and the Himalaya area are three hot-spot areas in the northern hemisphere. The eastern South Pacific, South Atlantic, South Africa, and Australia are hot spot areas in the southern hemisphere. These hot spot areas are also geographically consistent with the global distribution of desert areas.

During the northern hemisphere spring months (MAM), both $30°N$ and $20°S - 30°S$ latitudinal bands exhibit maximum ground-level O_3 concentrations.

During the northern hemisphere summer months (JJA), the $30°N$ and $20°S - 30°S$ latitudinal bands again present maximum ground-level O_3 concentrations.

However, the ground-level O_3 patterns over the North Atlantic and the northwestern Pacific show the northward intrusion of low O_3 from tropical latitudes, and southward transport of elevated O_3 from mid-latitudes. The atmospheric transport processes associated with the subtropical high circulations over the North Pacific and the North Atlantic, respectively, are responsible for the generation of these patterns during the northern hemisphere summer season.

During the northern hemisphere autumn months (SOP), both $30°N$ and $20°S - 30°S$ latitudinal bands remain to exhibit elevated O_3 concentrations on the ground.

The above results show that both $30°N$ and $20°S - 30°S$ latitudinal bands exhibit high impact from the tropopause regions. As such, these latitudinal bands are the areas which are less responsive to the tropospheric emissions and more susceptible to the transport processes in the tropopause regions.

Indeed, a followed up short-lived tracer experiment (experiment 28, Figure 9) confirms that $30°N$ and $20°S - 30°S$ latitudinal bands are more susceptible to the tropopause regions than other latitudinal bands.

doi:10.20944/preprints201706.0091.v1

The northern hemisphere continental areas (north of $30°N$), polar regions, and tropical continental regions all exhibit high ratios of O_3 simulated with the long-lived experiment to those O_3 calculated from the control run. These areas include North America, Euro-Asian continent, tropical South America Amazon regions, tropical central Africa, tropical South Atlantic, Indonesia, and Papua New Guinea regions. Hence these areas are more sensitive to the tropospheric emissions.

Further experiments with no stratospheric O_3 and NOy fluxes (Figure 10); and no stratospheric O_3 fluxes (Figure 11) all confirm the same results.

For all these experiments of stratospheric effects, the winter northern hemisphere is mostly dominated by the stratospheric processes, while the tropospheric emissions dominate over the southern hemisphere from tropics to $30°S$ regions. The northern hemisphere continental regions are increasingly dominated by tropospheric emissions from spring, to reach maxima in summer, and started to reduce in autumn months.

For the experiments with no industrial, biomass burning, and vegetation emissions (Figure 10); and no vegetation emissions (Figure 11), the northern hemisphere continental areas all exhibit consistent effects dominated by tropospheric emissions from spring to autumn months. The tropospheric emissions consistently dominate over the southern hemisphere continental regions from tropics to $30°S$.

4. Conclusions

In this work, we examined the effect of tropospheric emissions on tropospheric ozone (O_3) by conducting three-dimensional (3D) chemistry transport model (CTM) simulations. For the control run, the CTM model simulates tropospheric O_3 levels with a complete set of anthropogenic, biomass burning, and vegetation emissions. The pyrogenic emissions (biomass burning emissions from tropical and southern continents such as South America, Africa, and Southeast Asia) and anthropogenic emissions from fossil-fuel related combustions. For the no-emission simulation, all anthropogenic and biomass burning emissions were turned off. Comparisons of results from these two simulations exhibit the emission impacts on the tropospheric O_3. In the no-emission simulation, distinctive low surface O_3 with concentrations less than 5 ppbv prevail over the Amazon basin, tropical South America, tropical South Africa, Southeast Asia. Transport of air from these land areas downwind contributes to the low O_3 over the remote marine boundary layer. In contrast, elevated O_3 levels over the extra-tropical remote marine boundary layer are less supported by the anthropogenic and biomass burning emissions but more sustained by the downward transport of O_3 from the stratosphere. These results demonstrate that the northern hemisphere continental areas (north of $30°N$), polar regions, and tropical continental regions are more sensitive to the tropospheric emissions. The northern hemisphere winter is mostly dominated by the stratospheric processes, while the tropospheric emissions dominate over the southern hemisphere tropical continental areas from tropics to $30°S$ latitudinal bands. The northern hemisphere continental regions are increasingly dominated by tropospheric emissions from spring, to reach maxima in summer, and started to reduce in autumn months.

Acknowledgments

We thank British Atmospheric Data Centre (BADC) and European Centre for Medium-Range Weather Forecast (ECMWF) for meteorological analysis data used to run the IMS model; NASA SHADOZ project, S.J. Oltmans of CMDL/NOAA, and Taiwan Central Weather Bureau for the ozonesonde data. We thank D.E. Shallcross and J.A. Pyle for their support of this work. The results shown in this work was conducted by running the IMS model on a Cray J90 supercomputer at National Taiwan University (NTU). This research was supported by the NSC grant NSC-89-2119-M-008-007.

Author Contributions

The authors contribute equally to the reported work.

Conflicts of Interest

The authors declare no conflict of interest.

References

1. Wang, K.-Y.; Kau, W.-S. Kau. Simulation of impact from stratospheric ozone on global tropospheric ozone distribution with a chemistry transport model: A case study during the 1990-1991 period, *Asia-Pacific J. Atmos. Sci.*, **2015**, *51(2)*, 137–155.
2. Browell, E.V.; Fenn, M.A.; Butler, C.F.; Grant, W.B.; Clayton, M.B.; Fishman, J.; Bachmeier, A.S.; Anderson, B.E.; Gregory, G.L.; Fuelberg, H.E.; Bradshaw, D.; Sandholm, S.T.; Blake, D.R.; Heikes, B.G.; Sachse, G.W.; Singh, H.B.; Talbot, R.W. Ozone and aerosol distributions and air mass characteristics over the South Atlantic Basin during the burning season, *Journal of Geophysical Research*, **1996**, *101*, 24,043–24,068.
3. Jacob, D.J.; Heikes, B.G.; Fan, S.-M.; Logan, J.A.; Mauzerall, D.L.; Bradshaw, J.D.; Singh, H.B.; Gregory, G.L.; Talbot, R.W.; Blake, D.R.; Sachse, G.W. Origin of ozone and NOx in the tropical troposphere: A photochemical analysis of aircraft observations over the South Atlantic basic, *Journal of Geophysical Research*, **1996**, *101*, 24,235–24,250.
4. Logan, J.A. An analysis of ozonesonde data for the troposphere: Recommendations for testing 3-D models and development of a gridded climatology for tropospheric ozone, *Journal of Geophysical Research*, **1999a**, *104*, 16,115–16,149.
5. Marufu, L.; Dentener, F.; Lelieveld, J.; Andreae, M.O.; Helas, G. Photochemistry of the African troposphere: Influence of biomass-burning emissions, *Journal of Geophysical Research*, **2000**, *105*, 14,513–14,530.
6. Monks, P.S. A review of the observations and origins of the spring ozone maximum, *Atmospheric Environment*, **2000**, *34*, 3545–3561.
7. Lelieveld, J.; Dentener, F.J., What controls tropospheric ozone? *Journal of Geophysical Research*, **2000**, *105*, 3531–3551.
8. Wang, K.-Y., Shallcross, D.E. Modelling terrestrial biogenic isoprene fluxes and its potential impact on global chemical species using a coupled LSM-CTM model, *Atmospheric Environment*, **2000**, *34*, 2909–2925.

9. Jia, J.; et al. Tropospheric ozone maxima observed over the Arabian Sea during the pre-monsoon. *Atmospheric Chemistry and Physics*, **2017**, *17.8*, 4915.
10. Liu, J.; et al. Causes of interannual variability over the southern hemispheric tropospheric ozone maximum. *Atmospheric Chemistry and Physics*, **2017**, *17.5*, 3279.
11. Yienger, J.J.; Klonecki, A.A.; Levy II, H.; Moxim, W.J.; Carmichael, G.R. An evaluation of chemistry's role in the winter-spring ozone maximum found in the northern midlatitude free troposphere, *Journal of Geophysical Research*, **1999**, *104*, 3655–3667.
12. Wang, Y.; Logan, J.A.; Jacob, D.J. Global simulation of tropospheric O_3-NO_x-hydrocarbon chemistry 3. Origin of tropospheric ozone and effects of nomenthane hydrocarbons, *Journal of Geophysical Research*, **1998**, *103*, 10,757–10,767.
13. Jaffe, D.; Mahura, A.; Kelly, J.; Atkins, J.; Novelli, P.C.; Merrill, J. Impact of Asian emissions on the remote North Pacific atmosphere: Interpretation of CO data from Shemya, Guam, Midway and Mauna Loa, *Journal of Geophysical Research*, **1997**, *102*, 28,627–28,635.
14. Perry, K.D.; Cahill, T.A.; Schnell, R.C.; Harris, J.M. Long-range transport of anthropogenic aerosols to the National Oceanic and Atmospheric Administration baseline station at Mauna Loa Observatory, Hawaii, *Journal of Geophysical Research*, **1999**, *104*, 18,521–18,533.
15. Fishman, J.; Minnis, P.; Reichle Jr., H.G. The use of satellite data to study tropospheric ozone in the tropics, *Journal of Geophysical Research*, **1986**, *91*, 14,451–14,465.
16. Fishman, J.; Fakhruzzaman, K.; Cros, B.; Nganga, D. Identification of widespread pollution in the Southern Hemisphere deduced from satellite analyses, *Science*, **1991**, *252*, 1693–1696.
17. Diab, R.D.; Thompson, A.M.; Zunckel, M.; Coetzee, G.J.R.; Combrink, J.; Bodeker, G.E.; Fishman, J.; Sokolic, F.; McNamara, D.P.; Archer, C.B.; Nganga, D. Vertical ozone distribution over southern Africa and adjacent oceans during SAFARI-92, *Journal of Geophysical Research*, **1996**, *101*, No. D19, 23,823–23,833.
18. Thompson, A.M.; Pickering, K.E.; McNamara, D.P.; Schoeberl, M.R.; Hudson, R.D.; Kim, J.H.; Browell, E.V.; Kirchhoff, V.W.J.H.; Nganga, D. Where did tropospheric ozone over southern Africa and the tropical Atlantic come from in October 1992? Insights from TOMS, GTE TRACE A, and SAFARI 1992, *Journal of Geophysical Research*, **1996**, *101*, 24,251–24,278.
19. Roelofs, G.-J.; Lelieveld, J. Model study of the influence of cross-tropopause O_3 transport on the tropospheric O_3 levels, *Tellus*, **1997**, *49B*, 38–55.
20. Roelofs, G.-J.; Lelieveld, J.; von Dorland, R. A three-dimensional chemistry/general circulation model simulation of anthropogenically derived ozone in the troposphere and its radiative climate forcing, *Journal of Geophysical Research*, **1997**, *102*, 23,389–23,401.
21. Wang, K.-Y.; Pyle, J.A.; Shallcross, D.E. Formulation and evaluation of IMS, an interactive three-dimensional tropospheric chemical transport model 1. Model emission schemes and transport processes, *Journal of Atmospheric Chemistry*, **2001a**, *38*, 195–227.
22. Wang, K.-Y.; Pyle, J.A.; Shallcross, D.E.; Lary, D.J. Formulation and evaluation of IMS, an interactive three-dimensional tropospheric chemical transport model 2. Model chemistry and comparison of modelled CH_4, CO, and O_3 with surface measurements, *Journal of Atmospheric Chemistry*, **2001b**, *38*, 31–71.

23. Berntsen, T.K.; Isaksen, I.S.A. A global three-dimensional chemical transport model for the troposphere. 1. Model description and CO and ozone results, *Journal of Geophysical Research*, **1997**, *102*, 21,239-21,280.
24. Wang, K.-Y.; Lary, D.J.; Hall, S.M. Improvement of a 3D CTM and a 4D variational data assimilation on a vector machine CRAY J90 through a multitasking strategy *Computer Physics Communications*, **2000**, *125*, 142–153.
25. Müller, J.-F.; Brasseur, G. IMAGES: A Three-Dimensional Chemical Transport Model of the Global Troposphere, *Journal of Geophysical Research*, **1995**, *100*, 16,445-16,490.
26. Murphy, D.M.; Fahey, D.W. An estimate of the flux of stratospheric reactive nitrogen and ozone into the troposphere, *Journal of Geophysical Research*, **1994**, *99*, 5325–5332.
27. Moody, J.L.; Oltmans, S.L.; Levy II, H.; Merrill, J.T. Transport climatology of tropospheric ozone: Bermuda, 1988-1991, *Journal of Geophysical Research*, **1995**, *100*, 7179–7194.
28. Oltmans, S.J.; Levy II, H.; Merrill, J.M.; Moody, J.L.; Lathrop, J.A.; Cuevas, E.; Trainer, M.; O'Neill, M.S.; Prospero, J.M.; Vömel, H.; Johnson, B.J. Summer and spring ozone profiles over the Atlantic from ozonesonde measurements, *Journal of Geophysical Research*, **1996**, *101*, 29,179–29,200.
29. Kajii, Y.; Akimoto, H.; Komazaki, Y.; Tanaka, S., Mukai, H.; Murano, K.; Merrill, J.T. Long-range transport of ozone, carbon monoxide, and acidic trace gases at Oki Island, Japan, during PEM-West B / PEACAMPOT B campaign, *Journal of Geophysical Research*, **1997**, *102*, 28,637–28,649.
30. Crawford, J.; Davis, D.; Chen, G.; Bradshaw, J.; Sandholm, S.; Kondo, Y.; Liu, S.; Browell, E.; Gregory, G.; Anderson, B.; Sachse, G.; Collins, J.; Barrick, J.; Blake, D.; Talbot, R.; Singh, H. As assessment of ozone photochemistry in the extratropical western North Pacific: Impact of continental outflow during the late winter/early spring, *Journal of Geophysical Research*, **1997**, *102*, No. D23, 28,469–28,487.
31. Moody, J.L.; Oltmans, S.L.; Levy II, H.; Merrill, J.T. Transport climatology of tropospheric ozone: Bermuda, 1988-1991, *Journal of Geophysical Research*, **1995**, *100*, 7179–7194.

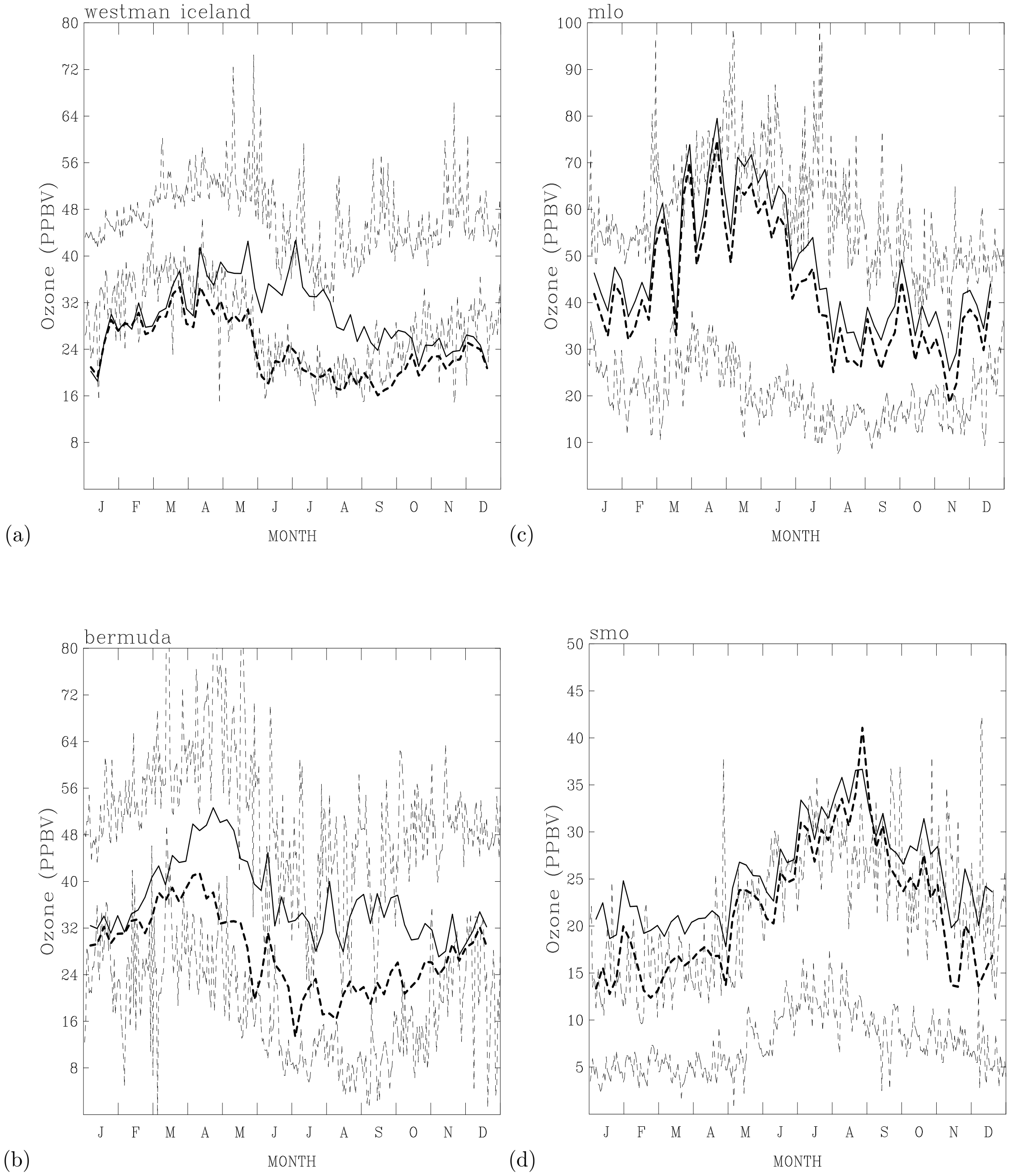

Figure 1. Comparison of two modeled seasonal cycles of O_3 (ppbv) calculated with (solid thin lines) and without (bold dashed lines) emissions included in the model at (a) Westman, Iceland $(63.4°N, 20.3°W)$, (b) Bermuda $(32°N, 65°W)$, (c) Mauna Loa $(19.5°N, 155.6°W)$, and (d) Samoa $(12.3°S, 170.6°W)$ with the measurements (thin dashed lines). Two measured O_3 levels for the period 1988-1992 (except at Westman where the 1992-1997 data were used) are shown here, one for the daily maximum, while the other one for the daily minimum.

doi:10.20944/preprints201706.0091.v1

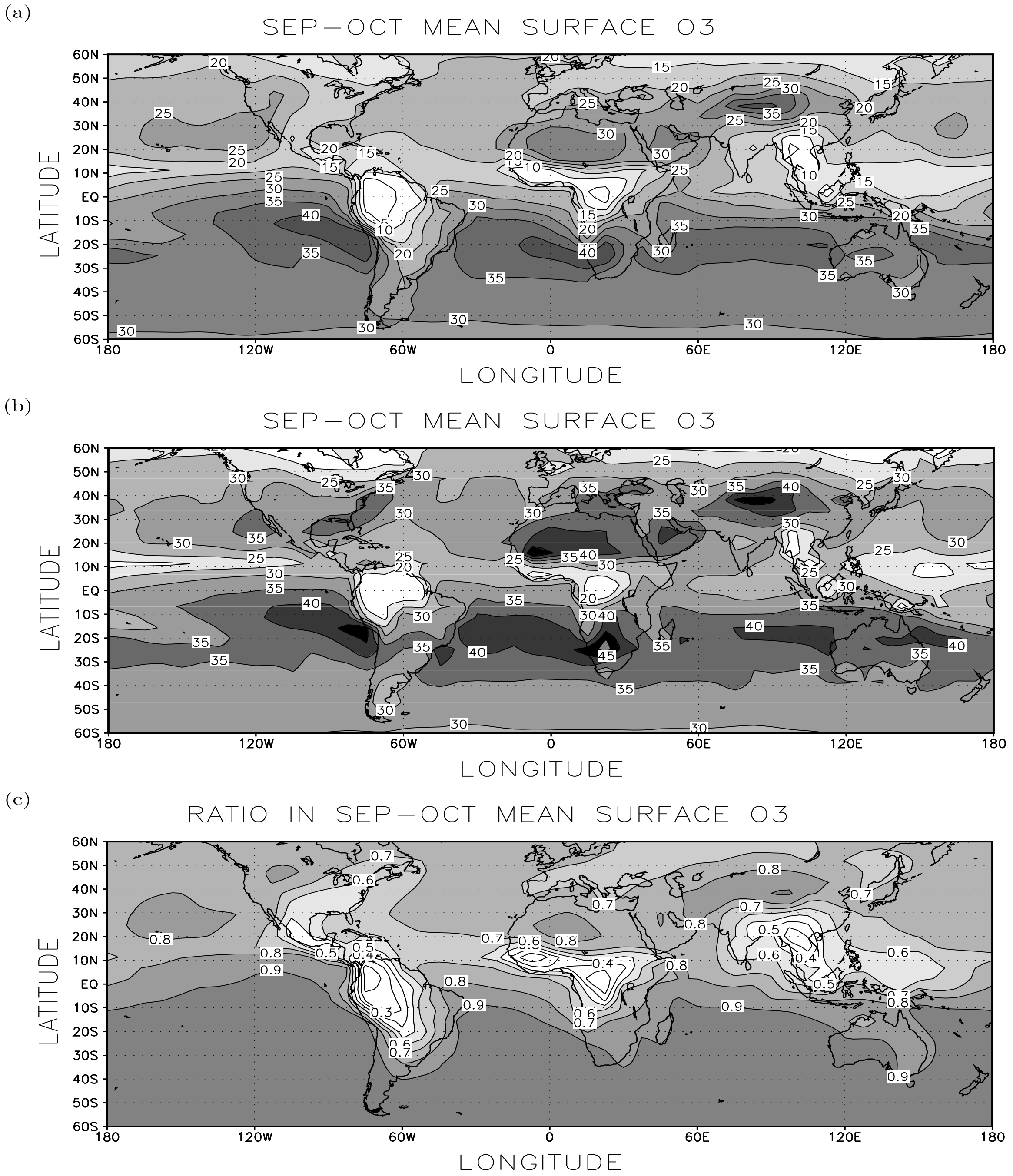

Figure 2. September to October mean ozone distributions (ppbv) simulated for (a) without and (b) with combustion emissions included in the model [1]; and (c) ratio of O_3 between (a) and (b).

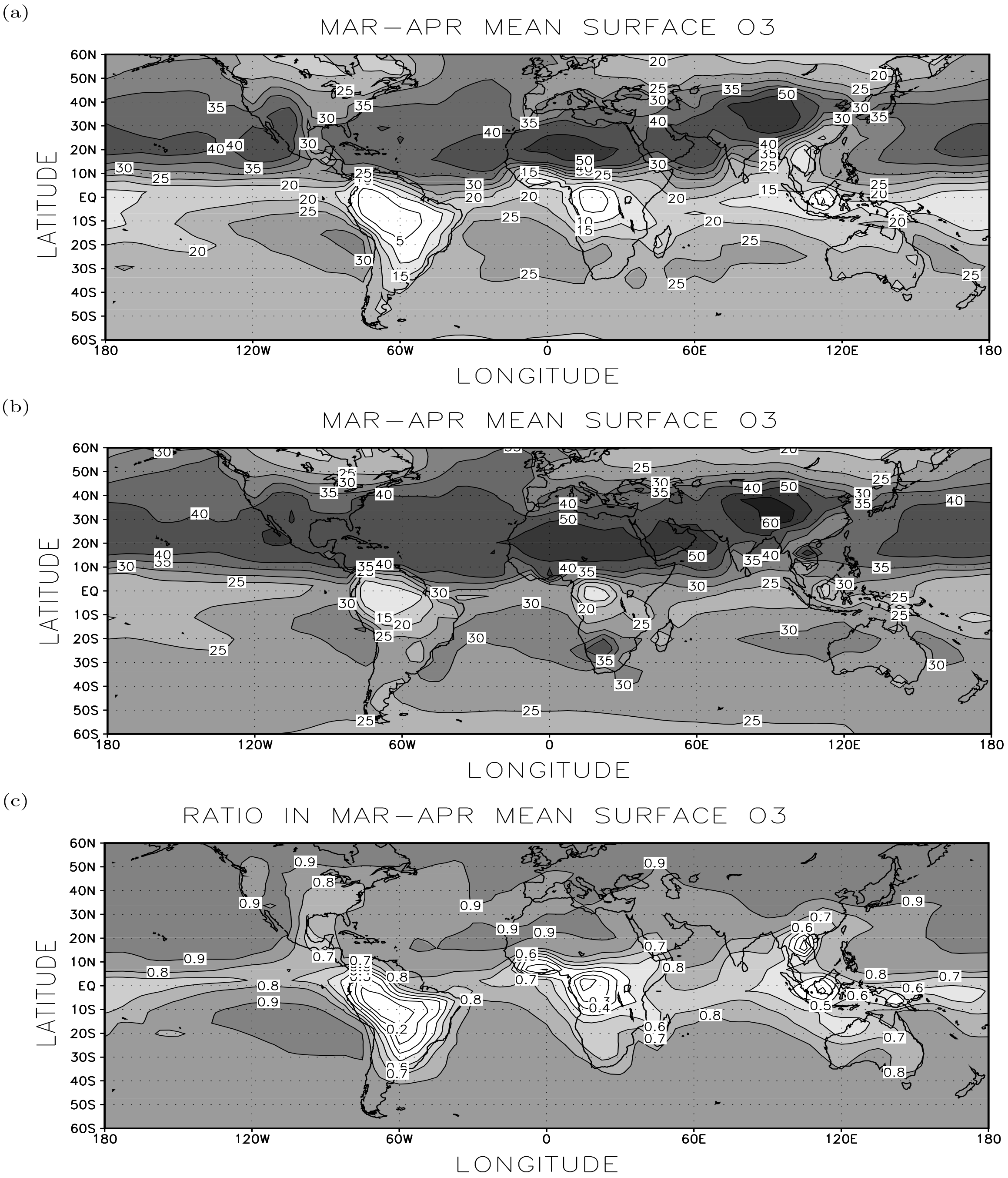

Figure 3. March to April mean ozone distributions (ppbv) simulated for (a) without and (b) with combustion emissions included in the model [1]; and (c) ratio of O_3 between (a) and (b).

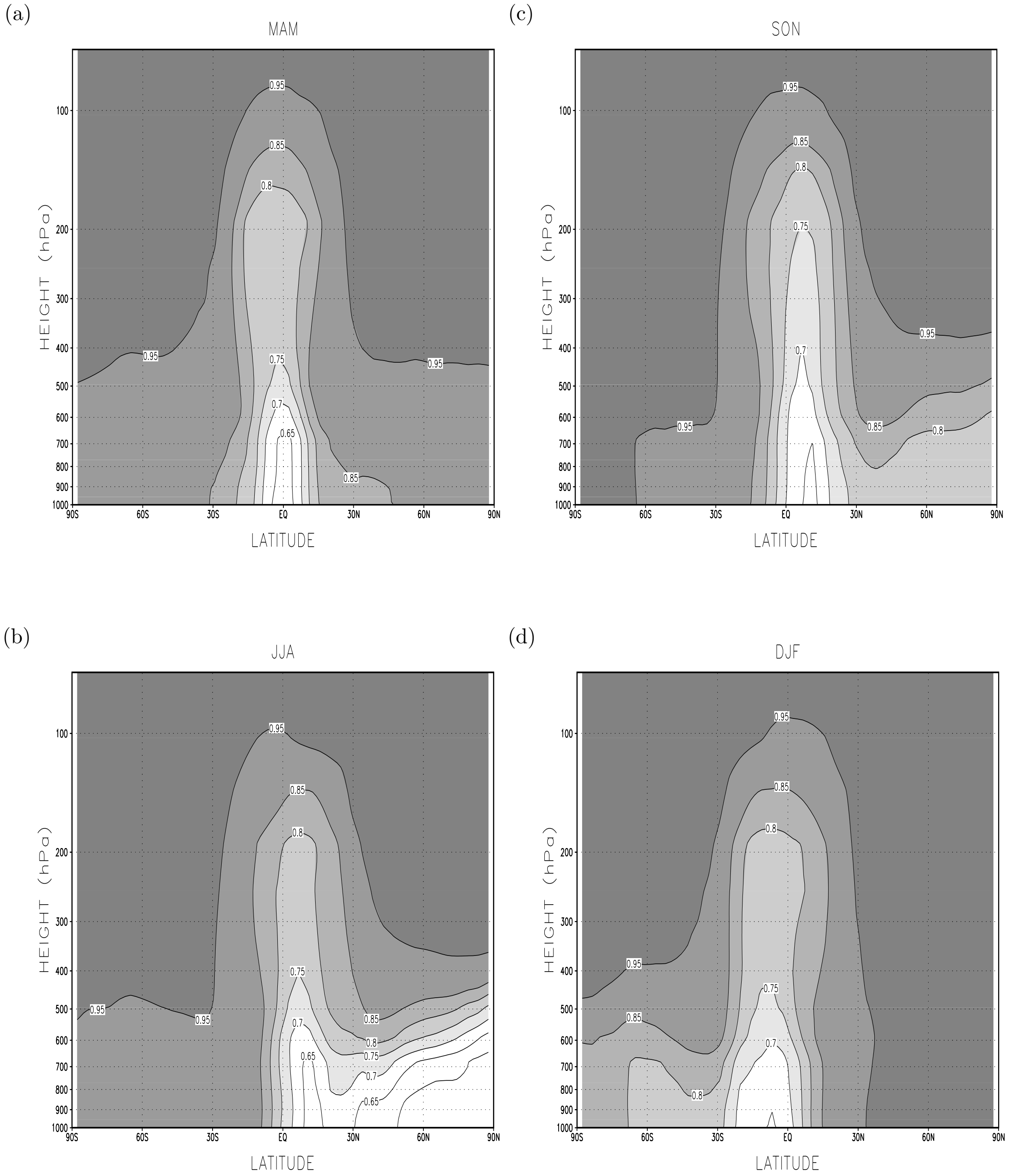

Figure 4. Zonal mean cross-section of ratio of O_3 simulated without to those with combustion emissions included in the model for (a) March, April, and May, (b) June, July, and August, (c) September, October, and November, (d) December, January, and February.

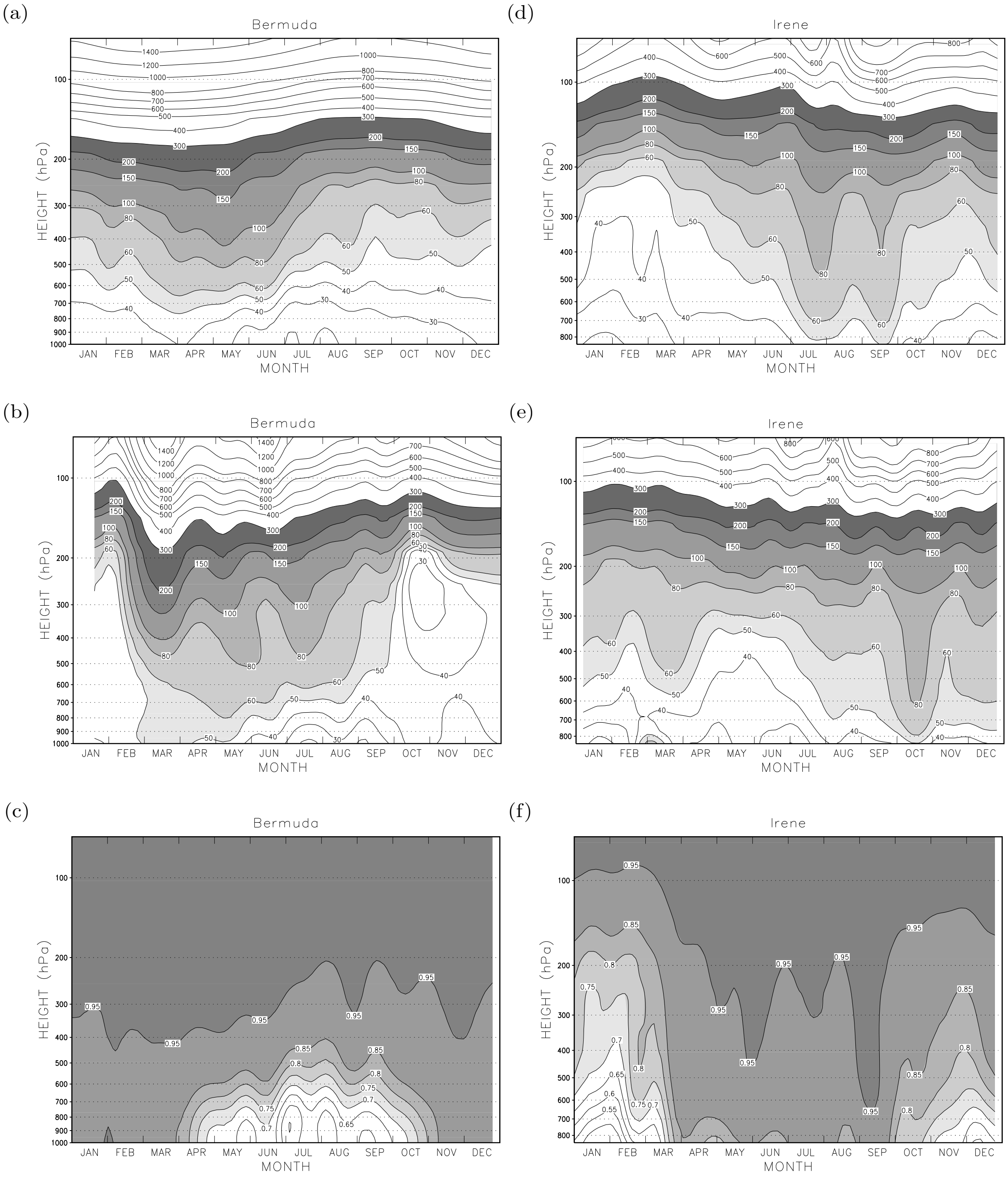

Figure 5. Time-height cross sections of O_3 (ppbv) simulated without combustion emissions included at Bermuda $(32°N, 65°W)$ (a) and Irene $(25.9°S, 28.2°E)$ (d); (b) and (e) show ozonesode measurements [1]; (c) and (f) show ratio of O_3 simulated without to those with combustion emissions included in the model.

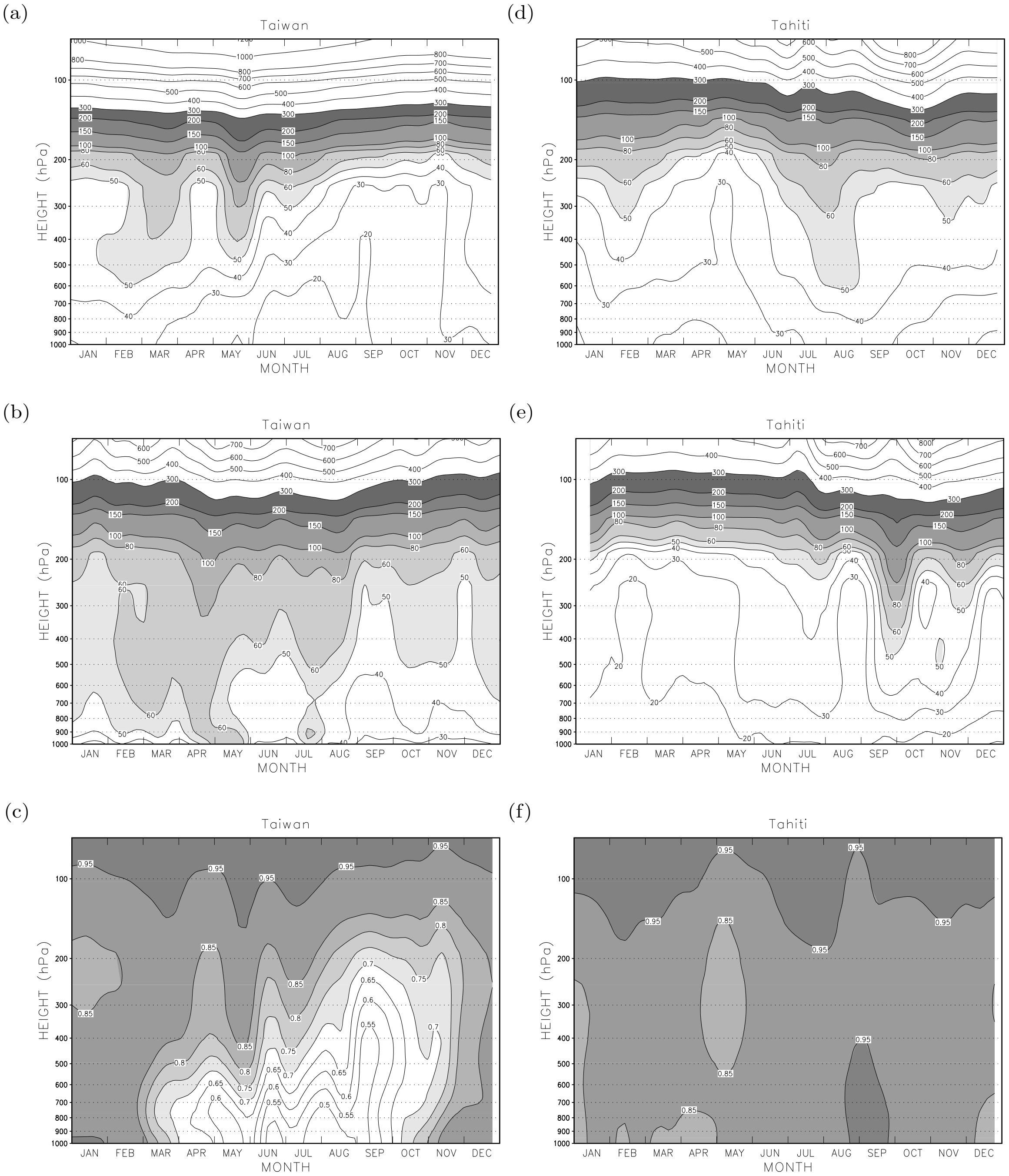

Figure 6. Time-height cross sections of O_3 (ppbv) simulated without combustion emissions included at Taiwan $(25^\circ N, 121^\circ E)$ (a) and Tahiti $(18^\circ S, 150^\circ W)$ (d); (b) and (e) show ozonesonde measurements [1]; (c) and (f) show ratio of O_3 simulated without to those with combustion emissions included in the model.

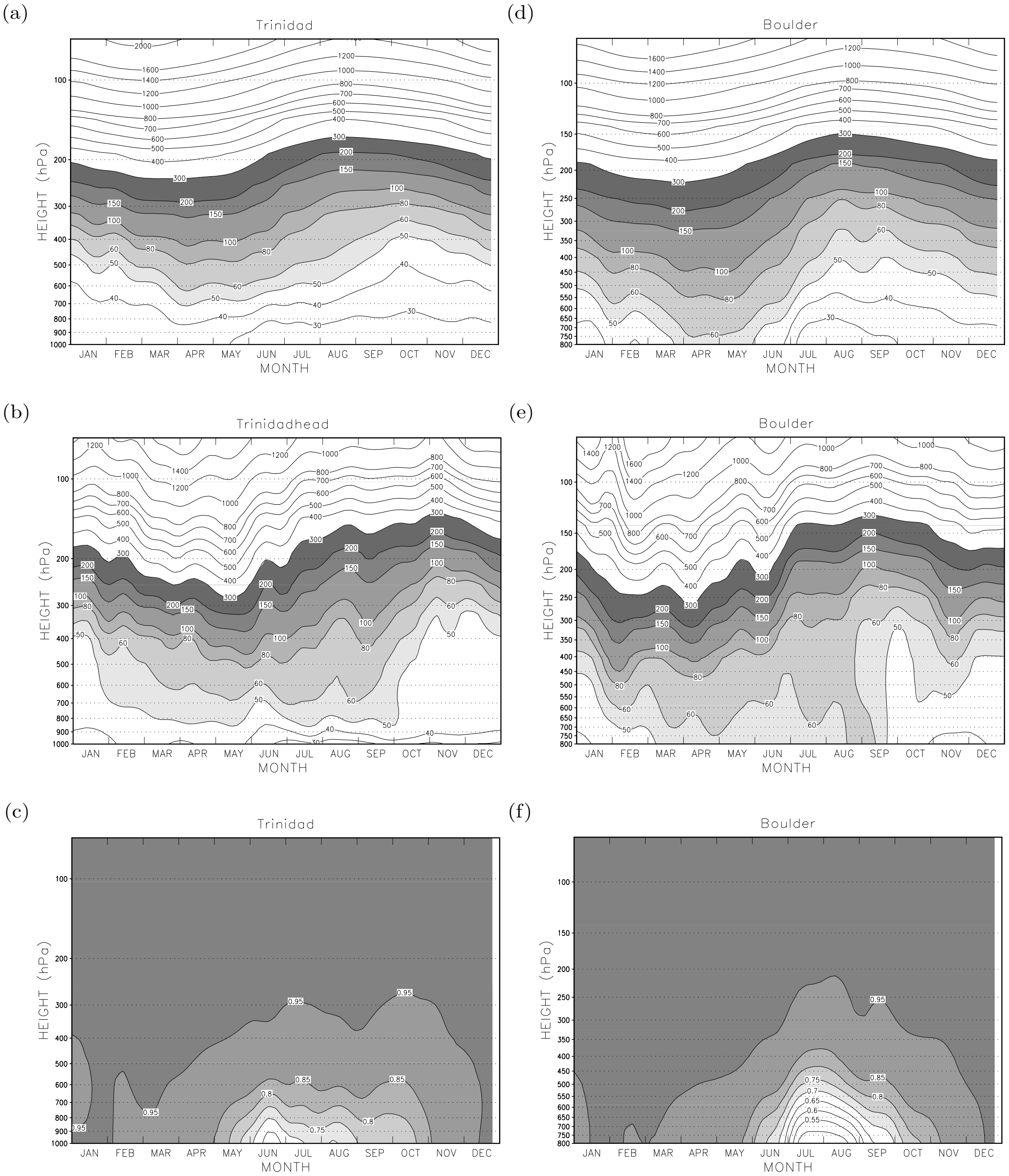

Figure 7. Time-height cross sections of O_3 (ppbv) simulated without combustion emissions included at Trinidad Head $(41.1°N, 124.2°W)$ (a) and Boulder $(40°N, 105°W)$ (d); (b) and (e) show ozonesonde measurements; (c) and (f) show ratio of O_3 simulated without to those with combustion emissions included in the model.

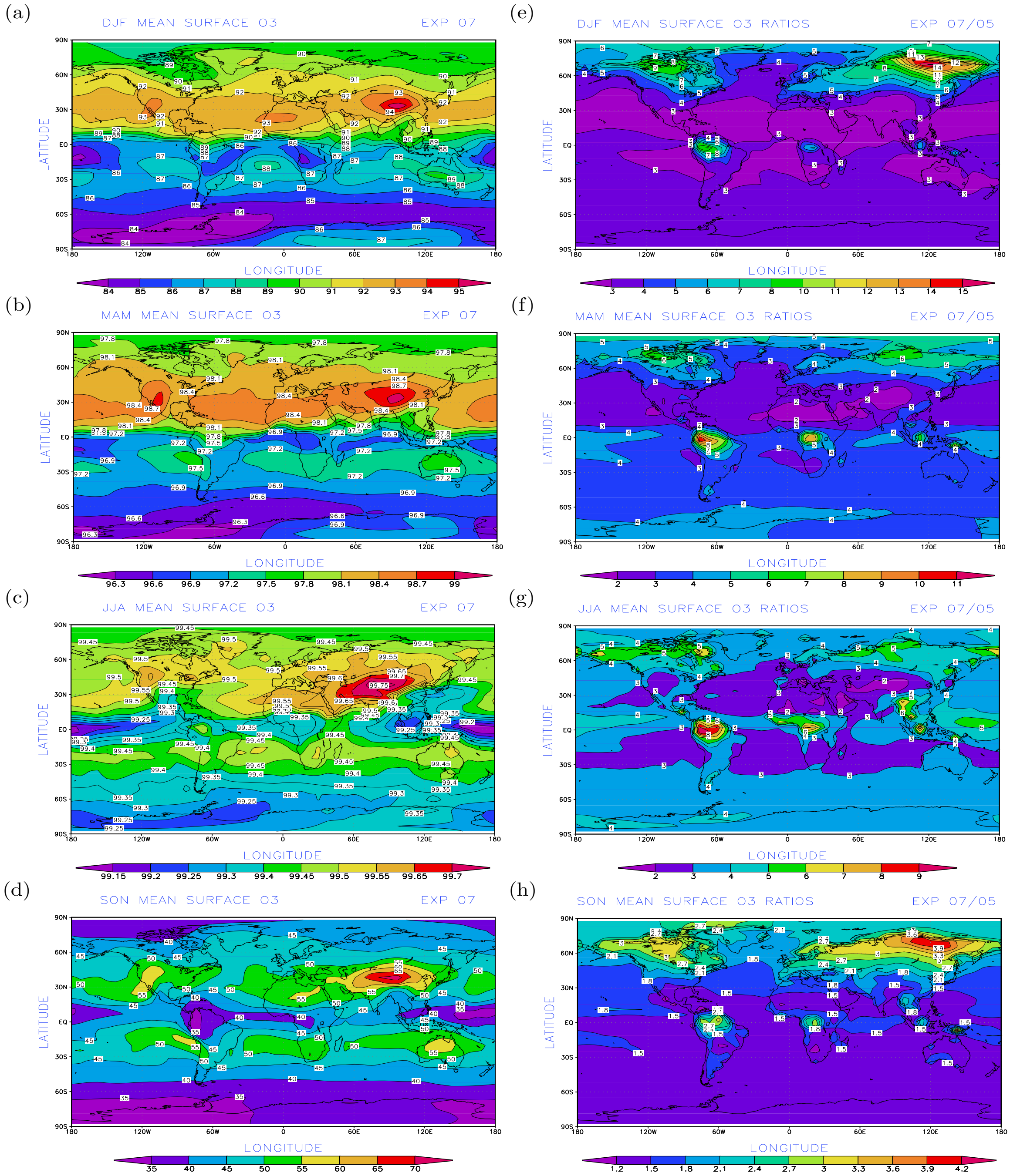

Figure 8. Seasonal mean ground-level O_3 concentrations (a-d) from long-lived tracer experiment; and ground-level O_3 ratios (O_3 from long-lived simulation to those from control run; e-h). (a) and (e) are Winter DJF (December, January, February) months. (b) and (f) are spring MAM (March, April, May) months. (c) and (g) are summer JJA (June, July, August) months. (d) and (h) are autumn SON (September, October, November) months.

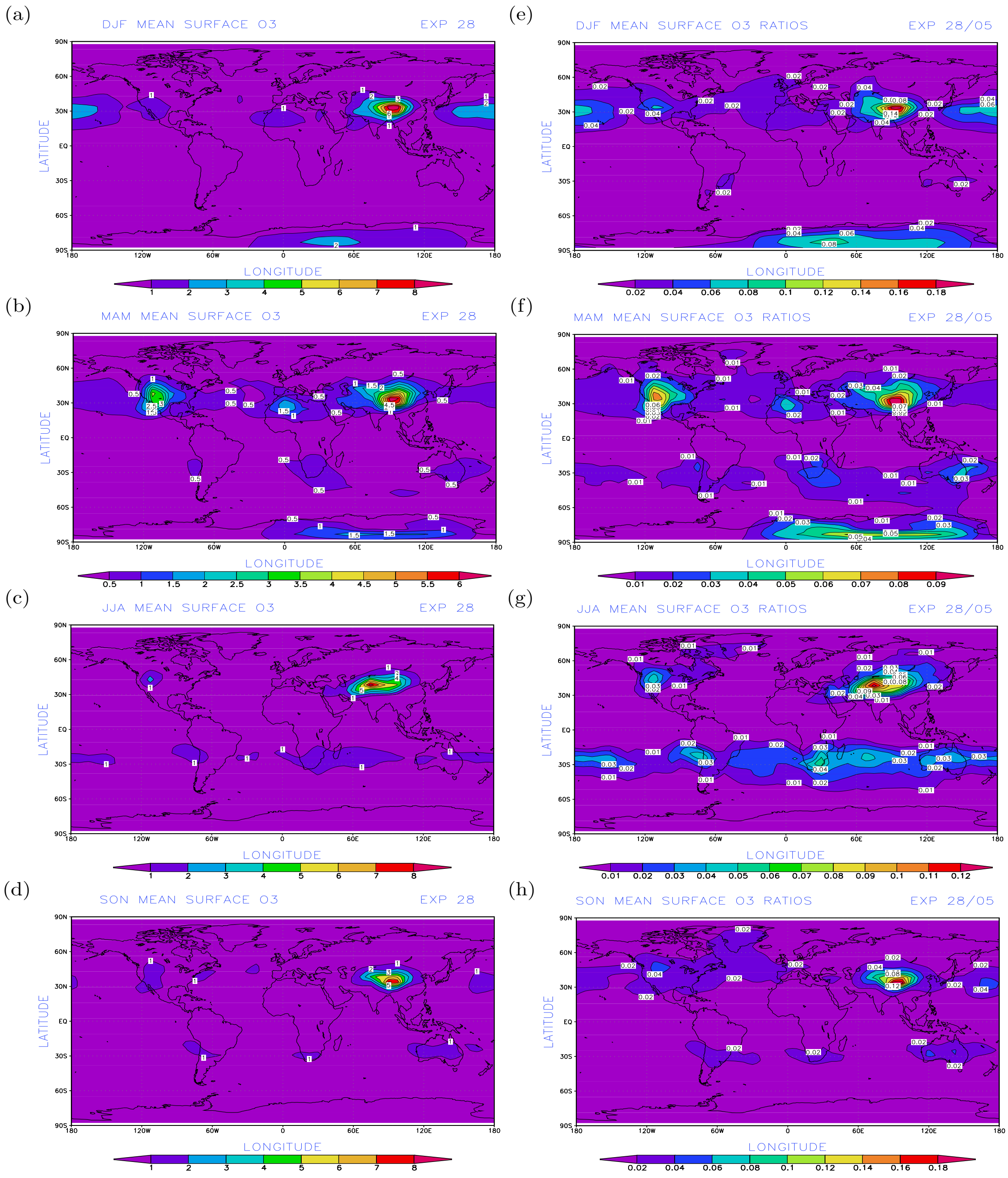

Figure 9. Seasonal mean ground-level O_3 concentrations (a-d) from short-lived tracer experiment; and ground-level O_3 ratios (O_3 from long-lived simulation to those from control run; e-h). (a) and (e) are DJF months. (b) and (f) are MAM months. (c) and (g) are JJA (June, July, August) months. (d) and (h) are SON months.

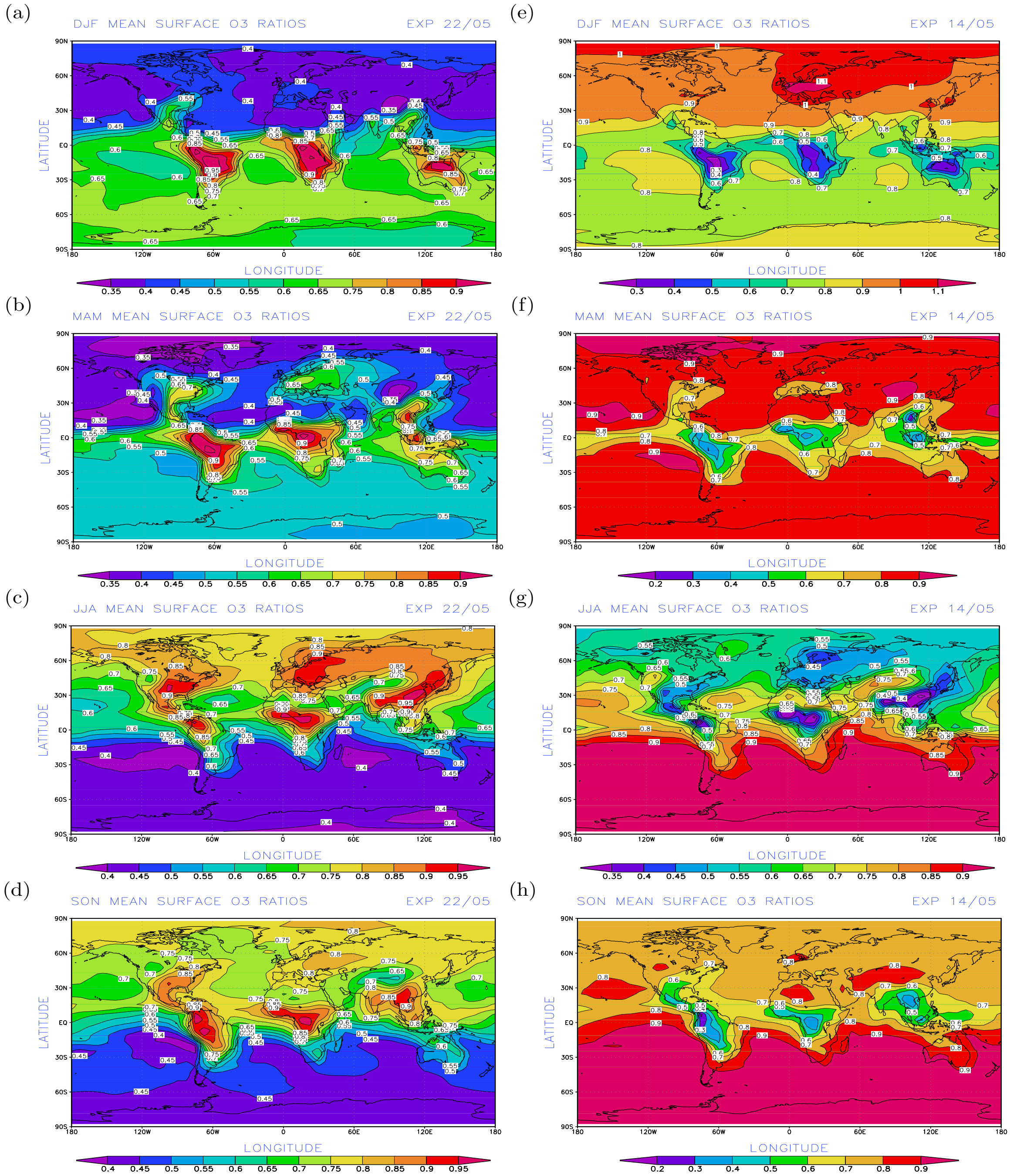

Figure 10. Seasonal mean ground-level O_3 ratios from a simulation without stratospheric $_{O}3$ and NOy fluxes to control run (a-d); and ground-level O_3 ratios from a simulation without tropospheric industrial, biomass burning, and vegetation emissions to control run (e-h). (a) and (e) are DJF months. (b) and (f) are MAM months. (c) and (g) are JJA (June, July, August) months. (d) and (h) are SON months.

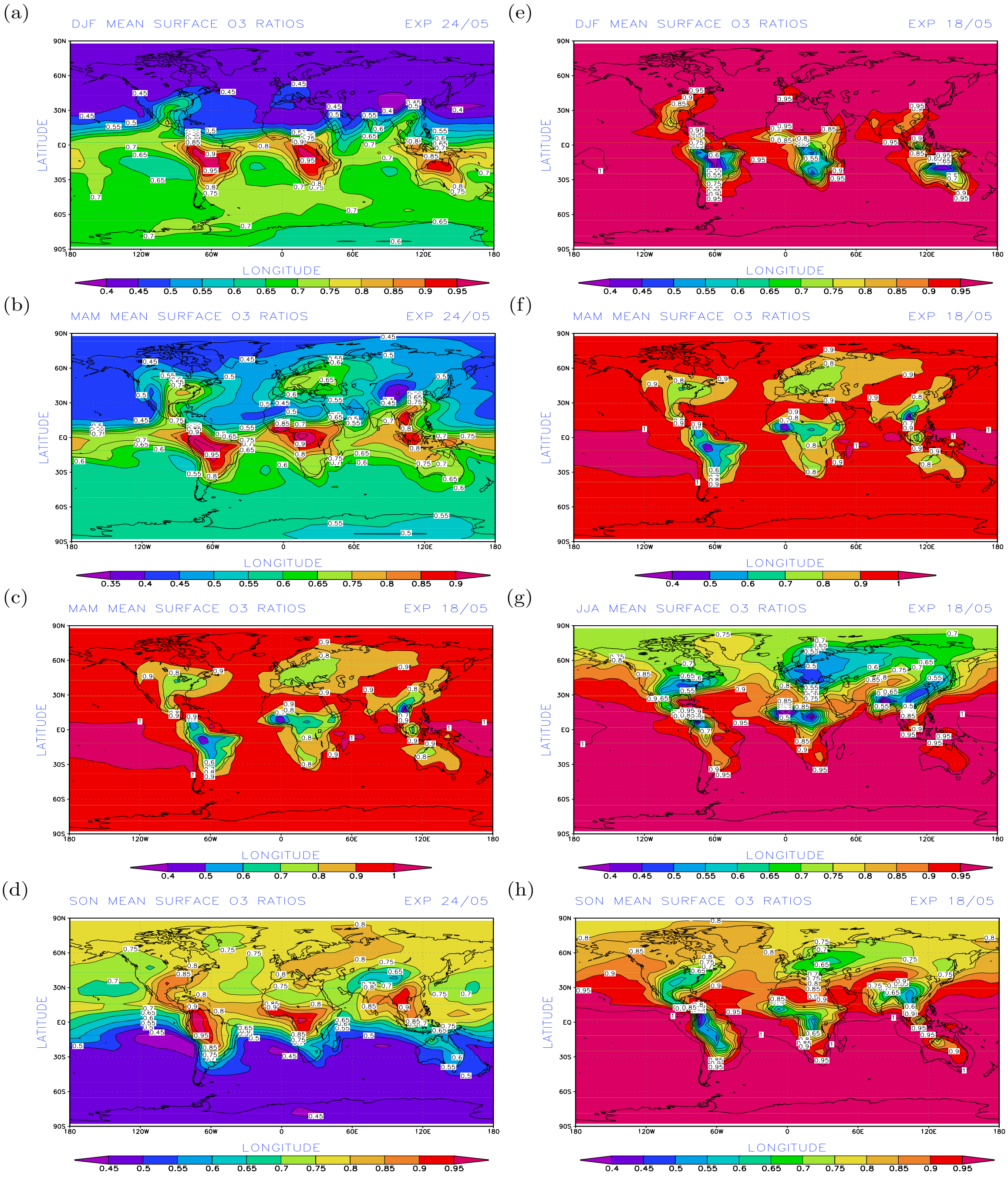

Figure 11. Seasonal mean ground-level O_3 ratios from a simulation without stratospheric ${}_{O}3$ fluxes to control run (a-d); and ground-level O_3 ratios from a simulation without tropospheric vegetation emissions to control run (e-h). (a) and (e) are DJF months. (b) and (f) are MAM months. (c) and (g) are JJA (June, July, August) months. (d) and (h) are SON months.